

Tomo-PIV Measurements Inside a Helically Coiled Tube

Fabio J. W. A. Martins^{1*}, Péter Kováts¹, Dominique Thévenin¹,
Katharina Zähringer¹

¹ Institute of Fluid Dynamics and Thermodynamics (ISUT),
Otto von Guericke University Magdeburg, Germany

* fabio.martins@ovgu.de

Abstract

In the current work, we present original 3D-3C averaged velocity measurements by means of tomographic particle image velocimetry (tomo-PIV) in a horizontally-coiled helical tube for Reynolds numbers ranging from 15 to 3646 and Dean numbers from 7 to 1719. Two velocity evaluations are compared: time average from instantaneous velocity fields and cross-correlation from an ensemble of instantaneous reconstructed volumes. Equivalent velocity field accuracy is obtained in both velocity approaches when the flow can be considered stationary. Results show full flow establishment after the first coil and secondary flow pattern with a pair of Dean vortices for most of the studied Reynolds numbers, in good agreement with the literature. The measured velocity fields can also be used for validation purposes of numerical models in computational fluid dynamics.

1 Introduction

Reactors in the shape of helically coiled tubes are a relatively new reactor concept in industry, in order to get narrow residence time distributions and to enhance heat transfer, mass transfer and mixing (Vashisth et al., 2008). The coiling induces strong secondary flow pattern in the form of a pair of counter-rotating vortices, called Dean vortices (Vashisth et al., 2008). These vortices are linked to the Reynolds number (eq. 1), the Dean number (eq. 2) and the torsion-to-curvature ratio (eq. 3) (Germano, 1989).

The Reynolds number based on the hydraulic diameter is defined as:

$$Re = \frac{\rho u d}{\mu} \quad (1)$$

where ρ is the fluid density, u is the bulk velocity, d is the hydraulic diameter and μ is the dynamic viscosity.

The Dean number, relating the magnitudes of inertial and centrifugal forces to those of viscous forces, is obtained as:

$$De = Re \sqrt{\frac{d}{2R}} \quad (2)$$

where R is the coil radius.

And the torsion-to-curvature ratio is defined as:

$$\lambda = \frac{p/(R^2 + p^2)}{R/(R^2 + p^2)} = \frac{p}{R} \quad (3)$$

where $2\pi p$ is the coil pitch.

Investigations of these secondary flows have been mainly performed analytically (e.g. Germano, 1989) and using numerical computations (e.g. Tang et al., 2016; Mansour et al., 2018b,a). Optical velocity measurements are rarely found in the literature. Liou (1992) studied Dean vortices in helically coiled tubes with different torsion-to-curvature ratios and Reynolds numbers employing laser-sheet flow visualization

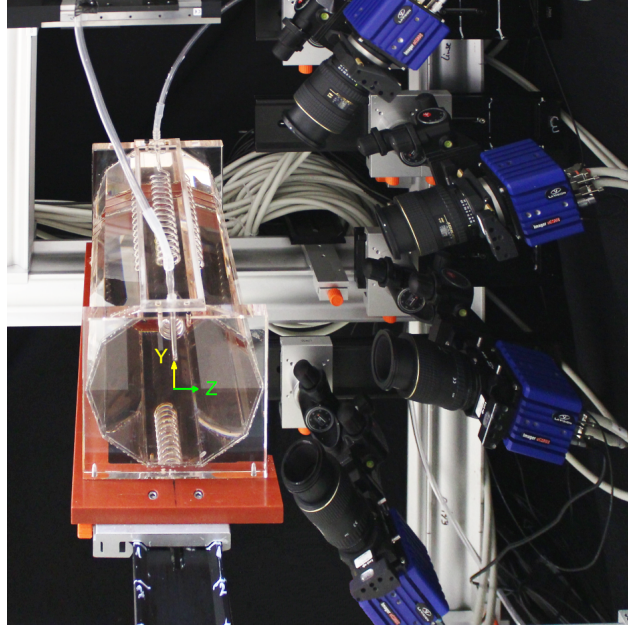


Figure 1: Experimental setup for tomographic PIV measurements. The helical coil here is filled with air to be visible.

and laser Doppler velocimetry. Later, Brito et al. (2016) used particle image velocimetry (PIV) to analyse the transient flow through a coiled pipe. While, Vester et al. (2016) investigated the turbulent swirling flows downstream a 90° pipe bend by means of hot-wire anemometry and stereoscopic PIV.

To optimize mixing in a helically coiled reactor, the detailed understanding of the flow dynamics is particularly important, and experimental data including velocity field measurements should be available to validate analytical models and computational simulations.

The present work provides original 3D-3C averaged velocity fields inside a horizontally positioned, helically coiled tube measured by tomographic particle image velocimetry (tomo-PIV) at different Reynolds numbers.

2 Experimental Setup

The test section consisted of a clear-glass helical coil with an inner diameter of $d \approx 6$ mm, a coil radius of $R \approx 13.7$ mm, a pitch of about 13.33 mm ($p \approx 2.12$ mm) and 15 coils. The torsion-to-curvature ratio was $\lambda \approx 0.15$. The helical tube was slightly elliptical due to the manufacturing coiling process of the glass. A straight pipe inlet with a length of about 125 mm allowed for flow development upstream the coiled region. The helically coiled pipe was horizontally installed inside an acrylic decagonal prism (Fig. 1). An ammonium-thiocyanate solution with a refractive index equal to the glass tube ($n = 1.468$) was used to fill the prism and as a working fluid. This refractive index matching technique strongly attenuated optical distortions. The properties of the ammonium-thiocyanate solution were $\rho = 1132$ kg/m³ and $\mu = 1.349$ mPa·s, which are close to those of the water. The fluid under investigation was driven by gravity, flowing from a tank located 1.5 m above the coil to a reservoir downstream the coiled tube. The flow rate was regulated by a roller clamp. A peristaltic pump returned the fluid from the reservoir to the tank, closing the loop.

The tomo-PIV setup was composed by a linear arrangement of four LaVision Imager sCMOS cameras (2560x2160 pixels @ 50 fps, pixel size 6.5×6.5 μm , 16 bit) equipped with 100-mm Tokina Macro lenses set with $f\#32$ apertures. A homogeneous volume illumination was obtained with 14 high-power COB Luminus LEDs (total nominal power of 1960 W) placed on the top, bottom, left and right side of the prism. White Vestosint 2178 polyamide particles (nominal diameter of 20 μm , $\rho = 1230$ kg/m³) were used as seeding tracers in the working fluid. The acquisition was synchronized by a programmable time unit driven by the LaVision DaVis 8.4 software, which was also used to calibrate and to process the data.

Acquisition of 1000 image pairs per camera was performed at a rate of 5 Hz for $Re \leq 1000$. For greater

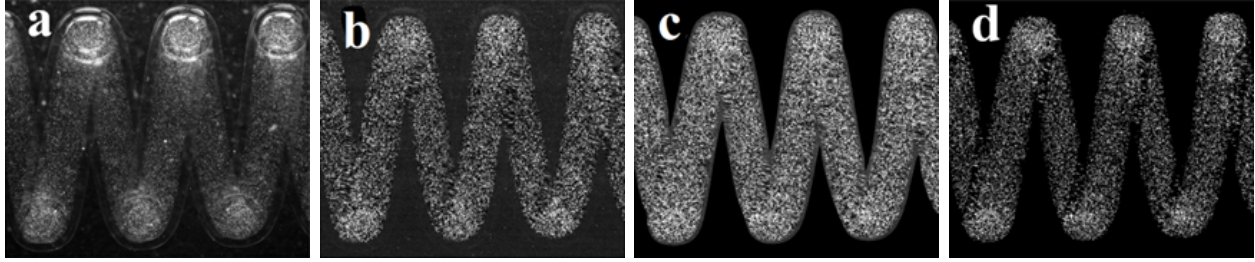


Figure 2: Exemplar images of the used pre-processing steps: (a) acquired image, (b) after time-moving-averaged background subtraction, (c) after masking out, and (d) after particle enhancement.

Reynolds numbers, the acquisition rate was increased to 10 Hz. The time delay between the acquisition pair was adjusted between 200 and 2000 μs , according to the flow rate, in order to optimize the maximum particle displacement to about 8 pixels.

The investigation region was divided into two fields of view to increase spatial resolution: from the straight tube inlet to the 2nd coil, and from the 3rd to the 5th coil. The decagonal prism was mounted on a rail to allow displacement of the helical coil for the two fields of view while the cameras remained fixed.

3 Tomo-PIV Calibration

A 3D calibration was performed in the first field of view for each investigated case. To this end, the helically coiled tube was removed and a 2D calibration target was placed inside the decagonal prism. Since the ammonium-thiocyanate solution is highly corrosive to metals, the calibration plate was made in polypropylene. The calibration plate was translated along the thickness of the coil by means of a traverse stage with 50- μm resolution. A total of 11 equally-spaced calibration planes from $Z = -20$ mm to $Z = 20$ mm were used for each calibration. The planes were composed of a dot-pattern Cartesian grid (3x3-mm grid resolution) covering the entire investigation region in all camera views. A pinhole fit function was employed to map physical coordinates into image coordinates.

The calibration was further refined by a self-calibration procedure (Raffel et al., 2018) for both fields of view and all cases separately. First the fluid inside the decagonal prism was stirred, resulting in a motion of few contaminants and spurious particles. A set of images was recorded. After, the helically coiled tube was inserted in the decagonal prism and a new set of images of the seeded working fluid flowing through the tube was recorded. Few iterations of self-calibration were performed with the combination of these two sets. The particle image density from the coiled tube flow was decreased by filtering out the low-intensity particles, in order to diminish spurious matchings in the disparity map. In each step, the obtained disparity fields were filtered and used to correct the current calibration. The final calibrations for the four cameras in all cases displayed root-mean-square triangulation errors below 0.1 pixel, which is the recommended limit for tomo-PIV (Raffel et al., 2018).

4 Tomo-PIV Processing

Images were pre-processed before volume reconstruction of the 3D particle intensity distributions. Fig. 2 shows the adopted pre-processing in an exemplar image from the 3rd to the 5th coil acquired by camera 1. The acquired image (Fig. 2a) displayed slight light reflections at the tube wall, mainly due to particle deposition, and small non-uniform illumination. These artefacts were firstly removed by using a 3-image-wide symmetrical moving average filter along the set (Fig. 2b). The resulted image had the background masked out (set to "0" intensity level) by a binarized image, created based on Gaussian and sliding minimum filters (Fig. 2c). This pre-processing step removed a big portion of the noise and slightly reduced the particle size in the images. Both effects are beneficial to decrease the amount of spurious particles ("ghost" particles) in the reconstructed volume (Martins et al., 2015). The particle images were further enhanced by applying a 5x5-pixel Gaussian smooth, followed by a sharpening filter, then by zeroing intensities below 8 counts, and finally by 10-fold intensity multiplication (Fig. 2d).

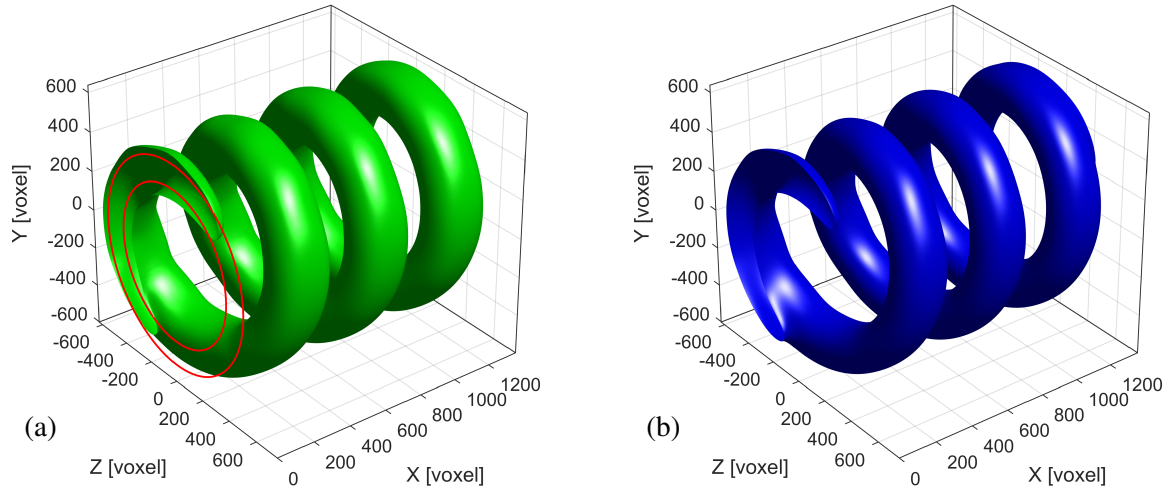


Figure 3: Example of (a) initial and (b) final helical masks for the reconstructed volumes of the second field of view. Legend: initial cylinder base (red lines), and isosurfaces of 0.05 (green) and 0.8 (blue).

Reconstructed volumes from the 4 camera images were obtained using the following steps. The volume was initialized with MinLOS, followed by 5 iterations of CSMART (fast and less-accurate version of SMART, Simultaneous Multiplicative Algebraic Reconstruction Technique) and then by 16 iterations of SMART. More information about these algorithms can be found in the book of Raffel et al. (2018). Volume smoothing with a strength of 0.5 and a volume threshold filter of 0.01 were enabled in the intermediate reconstruction steps.

A reduced reconstructed volume size of 1380x1238x1364 voxels was adopted due to our available 128GB-RAM computational power. To this end, a 2x2 binning was used in the pre-processed images to decrease their resolution before the volume reconstruction computation. In that way, the calculation of each volume reconstruction took about 40 minutes, while that of each instantaneous 3D vector field spent around 20 minutes.

In order to enhance the vector field quality, specially close to the helical walls, a 3D mask was applied in the reconstructed volumes prior to the vector field computation. This minimized the influence of ghost particles in the velocity vector calculation. It was not possible to create a 3D helical mask in DaVis 8.4 or by using a CAD software due to inaccuracies in the geometry of the helical coil, caused by the glass manufacturing process. The 3D mask based on the ensemble of reconstructed volumes of the particle distribution was generated using an in-house Matlab code as following. First, a cylinder extruded along the X-axis was employed to filter out particles outside its thickness. The cylinder base is displayed as red circles on the YZ-plane of Fig. 3a. Its inner and outer radii were obtained from projections of the ensemble of the reconstruction particle intensities onto the YZ-, XY- and XZ-planes. Second, particle intensities above a tiny threshold were set to "1", while others were set to "0". This minimizes the amount of ghost particles, which normally tend to have lower intensities (Raffel et al., 2018). The normalized volume was smoothed by a 20x20x20-voxel Gaussian filter to connect regions. Then, a low threshold was applied to obtain an initial mask of the approximate shape of the helix (Fig. 3a). Finally, this initial mask was smoothed and a final threshold, higher than the initial one, was used to generate a 3D mask with similar dimensions of those of the actual helically coiled tube (Fig. 3b). The present work adopted empirical thresholds of 0.05 and 0.8 for the initial and final helical masks, respectively. The 3D helical mask generated for each field of view was applied to the corresponding DaVis reconstructed volume files. The field "mask" was updated with the generated binary mask and the reconstructed intensities at regions out of the mask were set to "0".

For the velocity computation, pairs of 3D reconstructed volumes were divided into cubical interrogation volumes and a three-step direct volume cross-correlation between each corresponding interrogation volume was applied only inside the helical mask. The first step used a 4x4x4 binning and 48x48x48-voxel interrogation volumes within 2 iterations. The second step employed a 2x2x2 binning and 40x40x40-voxel interrogation volumes within 2 iterations. While the last step used 32x32x32-voxel interrogation volumes (no binning) within 4 iterations. A 75% of overlap was adopted in all steps. The final 3D velocity field had a spatial resolution of 8x8x8 voxels (i.e., 0.25 mm). The present work then adopted two different approaches to calculate the 3D-3C averaged velocity fields.

The first approach computed a time series of instantaneous velocity fields from pairs of 3D reconstructed volumes, and then time averaged these velocity vector fields. This approach is commonly used for tomo-PIV evaluation and its resulted vector field will be referred along the text as "time-averaged velocity".

The second approach was based on the ensemble cross-correlation analysis. We performed the 3D velocity calculation in a pair of ensemble volumes averaged along the first exposure and second exposure of the reconstructed volume series. This alternative approach reduces the processing time, because just one 3D velocity calculation is performed in order to obtain the 3D averaged velocity field. The resulted vector field using the second approach will be termed as "ensemble-volume velocity". Although in the present work we employed the same interrogation volume size in the averaged velocity fields from instantaneous volume pairs and ensemble volume pairs, the latter computation allows for an extra benefit that is the evaluation of the fluid flow at higher resolution because of the better intensity contrast in the volume. It is important to mention that this ensemble cross-correlation must only be applied when the flow is stationary and laminar. This approach is used for a long time in standard PIV with low particle image density recordings proving to be very efficient (Raffel et al., 2018). Nevertheless, to the best of our knowledge, this is the first time that the ensemble cross-correlation analysis is used in a tomo-PIV measurement.

The volume reconstructed quality was estimated based on the light intensity signal-to-noise ratio (Martins et al., 2015; Raffel et al., 2018). This method requires a top-hat-shape illumination, an uniform seeding in the investigation domain, and assess to a "dark" reconstructed region (non-illuminated region or without seeding particles). First, an ensemble-volume containing the reconstructed intensity was created time-averaging the instantaneous reconstructed volumes. Then, the "noise" from ghost particles was computed averaging the intensities within the inner diameter of the helical mask (Fig. 3), since no scattered light from actual particles was expected in this unseeded region. The "signal" was obtained by averaging the intensities within the helical mask. Finally, the signal-to-noise ratio was computed, dividing these two average values. The quantified signal-to-noise ratio in both fields of view was above 6 for all investigated cases, which is 3-fold greater than the recommended value for a good reconstruction quality (Raffel et al., 2018).

In the present measurements, higher amount of ghost particles in the reconstructed volumes are expected in regions close to the tube wall and in regions where the light path refracted more times though the tube interface (rear side of the helical coil). This would be a natural consequence of a slight variation of the refractive index due to the wide range of light wavelengths of the used LED (Martins et al., 2018), even using refractive index matching technique.

The uncertainties in the velocity fields were estimated based on the root-mean-square of the divergence (since an incompressible flow without error measurements must have zero divergence), as discussed by Martins et al. (2015). Lowest uncertainties were generally observed in the central part of the tube and highest uncertainties were close to the tube wall. The average uncertainties in the first field of view were typically lower than in the second, probably due to the calibration procedure. The average uncertainty of the time-averaged velocity fields of each studied case was below 0.17 voxel, while the uncertainty of the corresponding ensemble-volume velocity fields was about 2-fold greater. These are good levels of uncertainty considering the complex geometry under investigation.

5 Results

Five different flow rates were investigated in the present work (Table 1). For each case, 3D instantaneous volumes were reconstructed from every 10th image, in order to decorrelate the samples. Average velocity fields were computed in two manners: time-averaging 100 instantaneous velocity fields computed from instantaneous volume pairs, and evaluating the velocity from a single volume pair that was the ensemble of 100 instantaneous reconstructed volume pairs.

Table 1: Flow parameters of tomo-PIV cases.

Case	Q [mL/min]	u [m/s]	Re	De
1	5	2.95×10^{-3}	15	7
2	46	2.71×10^{-2}	136	64
3	72	4.25×10^{-2}	214	101
4	475	2.80×10^{-1}	1410	664
5	1228	7.24×10^{-1}	3646	1719

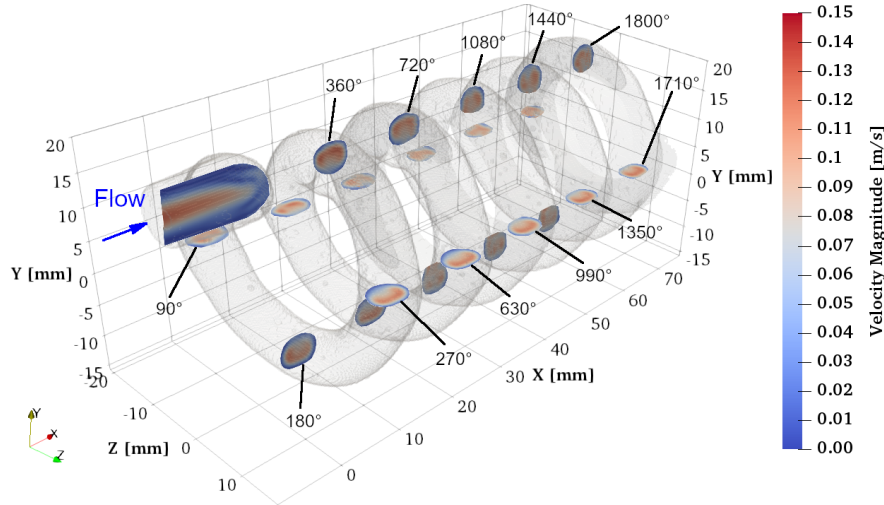


Figure 4: Time-averaged velocity inside the helical coil at $Re = 1410$, visualized by vector-magnitude colour at XY and XZ slices.

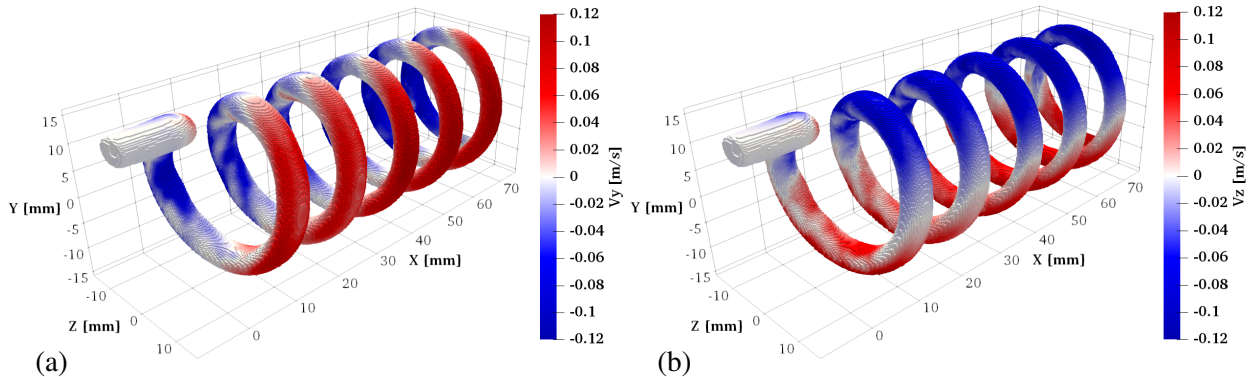


Figure 5: Time-averaged velocity close to the wall of the helical coil at $Re = 1410$: (a) Y -component and (b) Z -component.

Fig. 4 shows the 3D time-averaged velocity inside the horizontal helical tube from the inlet to the 5th coil for case 4 visualized by vector-magnitude at XY and YZ slices. It is possible to observe that the inlet flow is symmetric, while the flow along the curved tube is asymmetric, characterizing secondary motions.

Fig. 5 presents the Y and Z velocity components close to the tube wall for the same 3D field of Fig. 4. This figure is useful to examine the consistency of our tomographic volume reconstruction and velocity measurements, which are obtained from two fields of view that are joined together between the second and third turn of the helix.

The flow evolution of case 3 can be observed by the vector-magnitude colour of the ensemble-volume velocity fields in Fig. 6. In this figure, the rotation angle follows the helical revolution, starting at the inlet and increasing downstream the tube (Fig. 4). The flow velocity at the tube inlet is axisymmetric and agrees with that of a fully-developed laminar pipe flow. The flow then drastically changes due to the tube curvature. A dual peak distribution of the velocity magnitude, *quasi*-symmetric with respect to the vertical, is clearly visible after one-fourth of a revolution (90°). That is caused by secondary flows associated with vortices.

The length required for fully established conditions is linked to the Reynolds number and the torsion-to-curvature ratio. In Fig. 6, no significant changes seem to occur in the flow behaviour for positions downstream 270° . The small differences among these colour plots can reflect the stochastic nature of this flow and the present measurement uncertainties (which are slightly higher at 1350 and 1710°). For all cases, no significant differences are visible downstream the first coil. This is in agreement with the length required for fully established conditions obtained in the numerical simulations of Mansour et al. (2018a). They observed fully established flows after the first coil for a helical tube and Reynolds numbers similar to those of the present work.

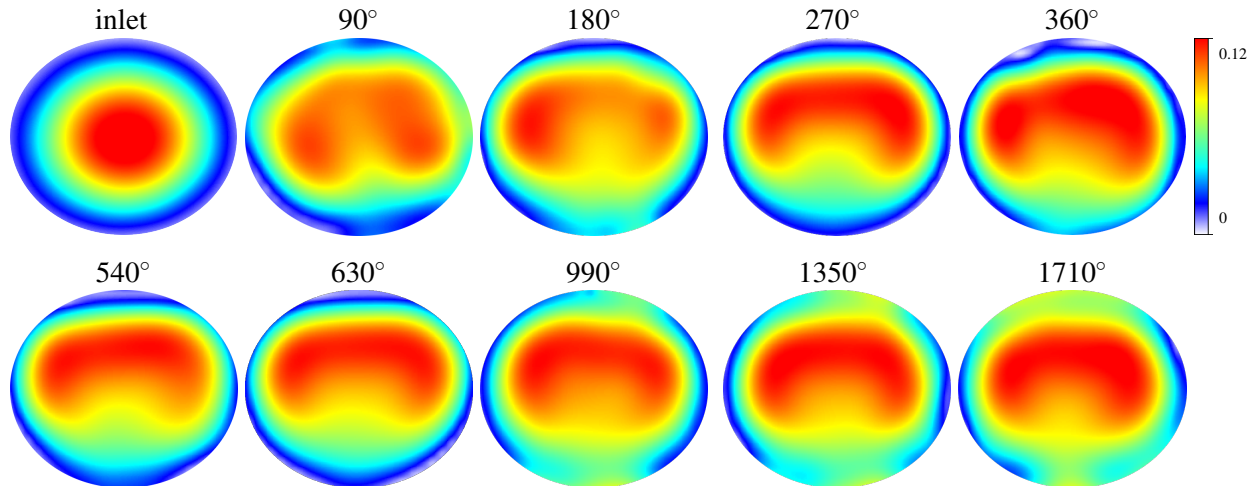


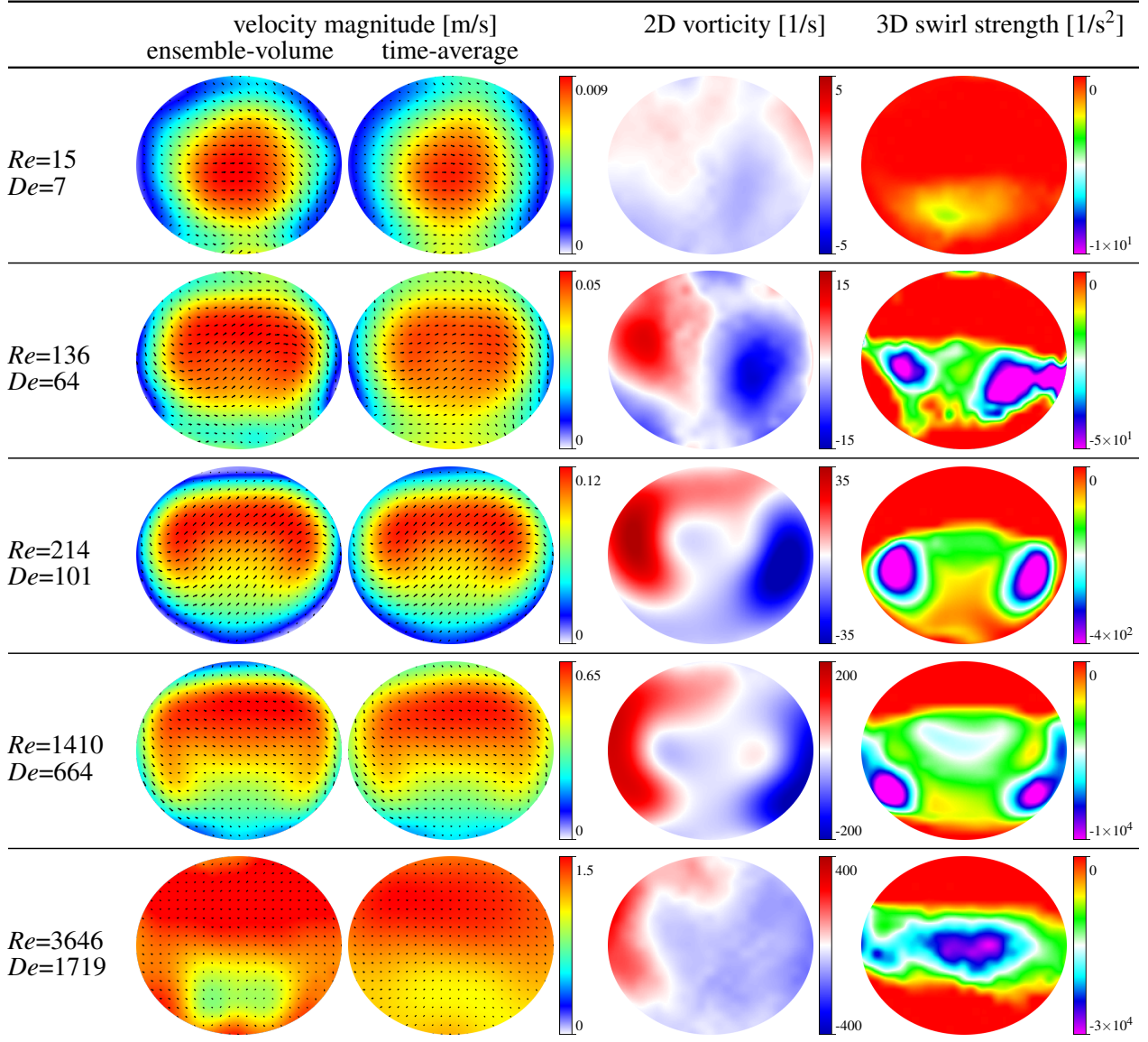
Figure 6: Colour plots of the evolution of the magnitude of the ensemble-volume velocity at cross-sections along the helically coiled tube at $Re = 214$.

Table 2 shows with more detail flows from $Re=15$ to 3646 inside the horizontally-coiled tube of the present work at the position 630° (i.e., after $1\frac{3}{4}$ turns). The flow is fully laminar at $Re=15$ (case 1) and starts to change at $Re=136$ (case 2). At $Re=136$ and $De=64$, a pair of vortices (see swirl strength field) appears due to the coiled tube. Then, these secondary flow structures evolve into stable structures. Dual-peak distributions become present and persistent in the velocity, out-of-plane vorticity and swirl strength fields for $Re=214$ and $De=101$ (case 3), and for $Re=1410$ and $De=664$ (case 4). A pair of strong vortices, the so-called Dean vortices, are easily identifiable by means of the 3D swirl strength criterion ($\hat{\lambda}_{ci}$), based on the velocity derivatives along all directions provided by tomo-PIV measurements. Although, out-of-plane vorticity also shows the presence of such vortices, their centres are better detected in the swirl strength criterion, which is able to differentiate shear from rotational motions. For the turbulent flow at $Re=3646$ (case 5), the velocity fields seem not fully converged with 100 samples. Nonetheless, the analysis of swirl strength fields reveals that the vortex pair appears to merge into a single vortex at $Re=3646$. It is also conjectured that this "single" vortex can be an artefact of the spacial resolution of the present measurements and would be actually a cluster of small intense vortices.

Similar secondary flow behaviour in the Dean region was observed in the experimental visualizations of Liou (1992) as well as in the numerical works of Tang et al. (2016) and Mansour et al. (2018b). Mansour et al. (2018b) investigated flows inside helical tubes with different geometries at a wide range of Reynolds numbers by means of numerical simulations. They also visualized a single strong vortex in some of their flows (e.g., flow at $Re=1000$ inside a helical coil with a 10-mm tube diameter, 70-mm coil diameter and 16-mm coil pitch). Nevertheless, a quantitative comparison between our results with those from the scarce literature was not possible, because of different helical coil geometries and flow parameters. Numerical simulations of the present conditions are currently being analysed and will be presented in a future article.

The comparison between ensemble-volume and time-average velocity fields of Table 2 for laminar (case 1) and Dean regimes (cases 3 and 4) are in good agreement. For other cases and also in regions of high velocity fluctuations (e.g. between Dean vortices), ensemble-volume velocity fields overestimate the velocity magnitude. This behaviour is expected because in these cases the flow was neither stationary nor laminar, which are recommended conditions for ensemble cross-correlation technique (Raffel et al., 2018). Close to the tube wall, corresponding to regions with low velocity magnitude and higher amount of ghost particles, the ensemble-volume method obtained better performance than the time-average method.

Table 2: Colour plots of ensemble-volume velocity, time-averaged velocity, out-of-plane vorticity and swirl strength (λ_{ci}) at 630° . In-plane components of the velocity vector are plotted in the velocity magnitude fields.



6 Conclusions

In the present experimental study, 3D-3C averaged velocity fields inside a horizontally-coiled helical tube from the inlet to the 5th coil were measured by means of tomographic particle image velocimetry. Refractive index matching technique was employed by using ammonium-thiocyanate solution as working fluid. A wide range of Reynolds numbers from 15 to 3646 (corresponding to Dean numbers from 7 to 1719) was investigated, covering laminar, transition, Dean and turbulent regimes.

Two velocity evaluation approaches were discussed: time average of instantaneous velocity fields, and cross-correlation of a pair of the ensemble of instantaneous reconstructed volumes. Good reconstructed volume quality and velocity field accuracy were obtained in both cases for this rather complicated geometry in terms of light paths. The two velocity approaches lead to similar fields for laminar and Dean regimes, when the flow can be considered stationary. Ensemble-volume approach is faster than the traditional time average, and, therefore, should be used more often in tomographic PIV measurements.

Flow field results inside the present helical tube show fully flow establishment after the first coil and stable secondary motions with the presence of pairs of vortices characterizing the Dean regime for $Re=214$ and $De=101$, and for $Re=1410$ and $De=664$. Results were in agreement with computational and experimental studies in the literature. The measured tomo-PIV velocity fields of the current work can be further used to validate numerical models and computational simulations especially for a systematic characterization of the influence of geometrical parameters and the role of Dean vortices on the heat and mass-transfer performance of helically coiled reactors.

Acknowledgements

The financial support of the DFG (German Research Foundation) in the frame of SFB/TR 63 project B1 is gratefully acknowledged. We thank the student Dávid Faragó for his participation in the experiments.

References

- Brito M, Sanches P, Ferreira R, and Covas D (2016) Experimental study of the transient flow in a coiled pipe using PIV. *Journal of Hydraulic Engineering* 143:04016087
- Germano M (1989) The dean equations extended to a helical pipe flow. *Journal of Fluid Mechanics* 203:289–305
- Liou T (1992) Flow visualization and LDV measurement of fully developed laminar flow in helically coiled tubes. *Experiments in fluids* 13:332–338
- Mansour M, Janiga G, Nigam K, Thévenin D, and Zähringer K (2018a) Numerical study of heat transfer and thermal homogenization in a helical reactor. *Chemical Engineering Science* 177:369–379
- Mansour M, Khot P, Thévenin D, Nigam KD, and Zähringer K (2018b) Optimal reynolds number for liquid-liquid mixing in helical pipes. *Chemical Engineering Science* DOI: 10.1016/j.ces.2018.09.046
- Martins FJWA, da Silva CC, Lessig C, and Zähringer K (2018) Ray-tracing based image correction of optical distortion for PIV measurements in packed beds. *Journal of Advanced Optics & Photonics* 1:71–94
- Martins FJWA, Foucaut JM, Thomas L, Azevedo LFA, and Stanislas M (2015) Volume reconstruction optimization for tomo-PIV algorithms applied to experimental data. *Measurement Science and Technology* 26:1–17
- Raffel M, Willert CE, Scarano F, Kähler CJ, Wereley ST, and Kompenhans J (2018) *Particle Image Velocimetry*. Springer. 3rd edition
- Tang L, Tang Y, and Parameswaran S (2016) A numerical study of flow characteristics in a helical pipe. *Advances in Mechanical Engineering* 8:1–8
- Vashisth S, Kumar V, and Nigam KD (2008) A review on the potential applications of curved geometries in process industry. *Industrial & Engineering Chemistry Research* 47:3291–3337
- Vester AK, Sattarzadeh SS, and Örlü R (2016) Combined hot-wire and PIV measurements of a swirling turbulent flow at the exit of a 90 pipe bend. *Journal of Visualization* 19:261–273